ADVANCED FUNCTIONAL MATERIALS
www.afm-journal.de
www.MaterialsViews.com

Carbon-Stabilized High-Capacity Ferroferric Oxide Nanorod Array for Flexible Solid-State Alkaline Battery–Supercapacitor Hybrid Device with High Environmental Suitability

*Ruizhi Li, Yimeng Wang, Cheng Zhou, Chong Wang, Xin Ba, Yuanyuan Li, Xintang Huang, and Jinping Liu**

Iron oxides are promising to be utilized in rechargeable alkaline battery with high capacity upon complete redox reaction ($Fe^{3+} \rightleftharpoons Fe^0$). However, their practical application has been hampered by the poor structural stability during cycling, presenting a challenge that is particularly huge when binder-free electrode is employed. This paper proposes a "carbon shell-protection" solution and reports on a ferroferric oxide–carbon (Fe_3O_4–C) binder-free nanorod array anode exhibiting much improved cyclic stability (from only hundreds of times to >5000 times), excellent rate performance, and a high capacity of ≈7776.36 C cm^{-3} (≈0.4278 C cm^{-2}; 247.5 mAh g^{-1}, 71.4% of the theoretical value) in alkaline electrolyte. Furthermore, by pairing with a capacitive carbon nanotubes (CNTs) film cathode, a unique flexible solid-state rechargeable alkaline battery-supercapacitor hybrid device (≈360 µm thickness) is assembled. It delivers high energy and power densities (1.56 mWh cm^{-3}; 0.48 W cm^{-3}/≈4.8 s charging), surpassing many recently reported flexible supercapacitors. The highest energy density value even approaches that of Li thin-film batteries and is about several times that of the commercial 5.5 V/100 mF supercapacitor. In particular, the hybrid device still maintains good electrochemical attributes in cases of substantially bending, high mechanical pressure, and elevated temperature (up to 80 °C), demonstrating high environmental suitability.

1. Introduction

Nowadays the energy storage has become a global concern since it has a wide range of critical application fields and plays a vital role in the development of sustainable society. Among various electrochemical energy-storage devices, supercapacitors (SCs), and rechargeable batteries are mostly promising as power-type and energy-type candidates, respectively.[1–3] To combine the merits of SCs and batteries, a battery-supercapacitor hybrid system with both high energy and power densities has been proposed.[4–6] Recent years has witnessed great progress in fundamental research of hybrid energy-storage devices for large-scale applications such as electric vehicles, etc.[7,8] However, their role in smart portable and wearable electronics needs much more attention; in these applications the power sources should be miniaturized in dimensions with robust mechanical flexibility.[9] This aim has inspired intensive efforts to explore flexible, solid-state, and thin-film electrode-based SCs/Li ion batteries with great volumetric energy storage capability.[10–13] Despite this, great challenge still remains in developing new types of flexible solid-state hybrid energy storage devices based on low-cost and environmentally friendly electrode materials.

Transition metal oxides (TMOs) in general exhibit high electrochemical energy storage ability as electrode materials due to multielectron Faradic reactions. Among them, ferroferric oxide (Fe_3O_4) is particularly promising since it is cheap, environmentally benign, and much more conductive than other TMOs ($\sigma = 2 \times 10^4$ S m^{-1}).[14,15] On the basis of the possible variation of iron's valence states ($Fe^{3+} \rightleftharpoons Fe^0$), Fe_3O_4 has a high theoretical capacity of ≈346.5 mAh g^{-1} in alkaline aqueous solution, making it potentially attractive as anode material for alkaline batteries.[16] Nevertheless, such a theoretical value can only be realized upon complete redox reaction within a wide negative potential window (≤–1.3 V vs Ag/AgCl). Under this condition,

R. Li, Prof. J. Liu
School of Chemistry
Chemical Engineering and Life Science and
State Key Laboratory of Advanced Technology
for Materials Synthesis and Processing
Wuhan University of Technology
Wuhan, Hubei 430070, P. R. China
E-mail: liujp@whut.edu.cn
R. Li, Y. Wang, C. Zhou, C. Wang, X. Ba, Prof. X. Huang, Prof. J. Liu
Institute of Nanoscience and Nanotechnology
Department of Physics
Central China Normal University
Wuhan, Hubei 430079, P. R. China
Prof. Y. Li
School of Optical and Electronic Information
Huazhong University of Science and Technology
Wuhan 430074, P. R. China

DOI: 10.1002/adfm.201502265

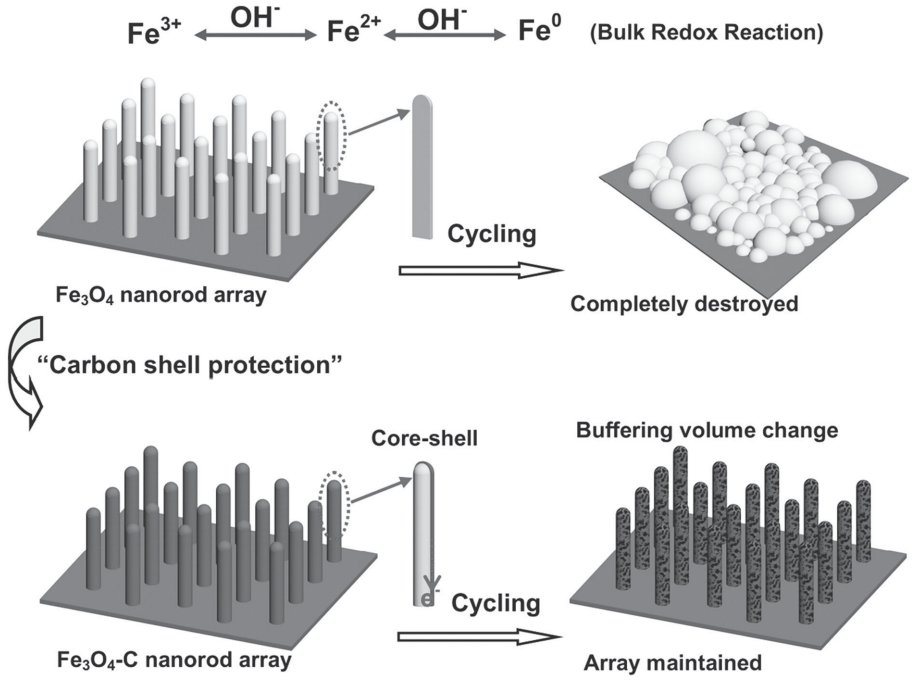

Figure 1. Schematic illustration of the functions of carbon shell on the stability improvement of Fe_3O_4 nanorod array during cycling.

the multiphase changes of iron oxides would cause huge volumetric expansion and structural deformation/dissolution, and electrolytic hydrogen evolution will be much more serious, which eventually lead to drastic capacity decay and ending after merely hundreds of cycles.[17,18] In order to address this issue, one popular way is to select relatively narrow working potential window to avoid too many phase-transition reactions, achieving the balance between capacity and cycling stability. For example, Shi et al. tested Fe_3O_4 nanoparticle electrode within a potential range of −0.8 to 0.2 V, but attained a capacity of only 28.9 mAh g^{-1}.[19] Much effort has also been made on mounting/dispersing nanosized Fe_3O_4 onto various carbonaceous materials such as carbon nanotubes/nanofibers/nanosheets, carbon black, carbon foam, and graphene, etc.[20–23] As expected, the strong covalent bonding with conductive carbon has potentially improved the electrochemical stability of Fe_3O_4 (mostly improved up to ≈1000 times). Despite great progress, challenge still remains in simultaneously obtaining high capacity, long cycling life and good rate capability, especially for thin-film iron oxide electrode in which the iron oxide nanostructures are grown directly on the current collector without any binder and additive for protection. In this case, the reported "carbon bonding/dispersion" method is also inapplicable for cycleability improvement. Since binder-free directly grown nanostructured electrodes are particularly promising for future flexible energy devices,[24–26] it is urgent to develop alternative way to address the cycleability issue of such Fe_3O_4 electrode architecture. In addition, matching of iron oxide alkaline battery anode with a pure capacitive cathode to assemble a flexible solid-state hybridized cell has never been considered but would be of great importance to the substantial advance in energy storage technology.

Herein, we put forward a "carbon shell-protection" solution and report a Fe_3O_4–carbon (Fe_3O_4–C) binder-free nanorod array anode that works well in alkaline electrolyte; we further construct a high-performance solid-state carbon nanotubes $(CNTs)_{(+)}//Fe_3O_4–C_{(-)}$ alkaline battery-supercapacitor hybrid device. Considering the relatively high electrical conductivity of spinel Fe_3O_4, the direct alignment of its nanorods on current collector would provide fast and direct electron transport channel and ensures robust electrical contact; the interspacing between nanorod individuals can further facilitate the electrolyte penetration and consequently reduce the interfacial resistance.[25–27] These make the ordered nanorod array architecture most efficient in terms of reaction kinetics. Nevertheless, in alkaline electrolyte, binder-free bare Fe_3O_4 array is much more fragile upon the complete redox reaction ($Fe^{3+} \rightarrow Fe^{2+} \rightarrow Fe^0$) during cycling, leading to rapid structural destruction, as illustrated in **Figure 1**. With carbon coating, a facile but versatile surface engineering protocol, the volume expansion that accounts for the structural deformation can be effectively buffered, helping maintaining the integration of nanorod array. The carbon shell would additionally improve the electrode conductivity. We have investigated in detail the influence of carbon concentration on the electrochemical performance of Fe_3O_4–C electrode. When optimized and activated, the Fe_3O_4–C array electrode exhibits full Fe valence state evolution with a high specific capacity of ≈247.5 mAh g^{-1} (7776.36 C cm^{-3}; 0.4278 C cm^{-2}) and the cycleability has been boosted to ≈5000 times (only hundreds of cycles for pristine Fe_3O_4 array electrode).

A solid-state alkaline battery-supercapacitor hybridized cell was further assembled by using optimized Fe_3O_4–C array as the battery-type anode, CNTs thin film as the capacitive cathode and polyvinyl alcohol (PVA)-KOH as the gel

electrolyte. The cell is fully binder-free, delivering high volumetric energy density approaching commercial Li thin-film batteries and high power density comparable to commercial SCs (1.56 mWh cm^{-3}; 0.48 W cm^{-3}). It also displays high environmental suitability in terms of substantially bending, high mechanical pressure and elevated temperature. Our work not only demonstrates a general approach to stabilize binder-free metal oxide nano array/film electrode for rechargeable alkaline battery, but also opens up an opportunity in developing multifunctional iron oxide-based hybrid energy storage systems.

2. Results and Discussion

2.1. Characterizations of the Fe_3O_4–C Nanorod Array

Fe_3O_4–C nanorod array electrode was fabricated by the adsorption of glucose onto pristine Fe_3O_4 nanorod array growing directly on a thin Ti foil with subsequent carbonization (see the Experimental Section for details). Top-view and cross-section scanning electron microscopy (SEM) images confirm that the generated film is made up of numerous vertically aligned nanorods with average diameter and length of ≈80 and 550 nm, respectively (**Figure 2**a,b). Some neighboring nanorods are fused together owing to the high-temperature carbonization process, giving rise to highly porous 3D electrode architecture. This structure would be much beneficial for electrolyte penetration. Optical image (inset in Figure 2b) illustrates that the uniform array film has robust mechanical adhesion to the current collector substrate even with serious bending. Typical transmission electron microscopy (TEM) analysis toward several Fe_3O_4–C nanorods is further displayed in Figure 2c. As shown, partially crystallized carbon shells can be easily found on the surface of nanorods, with average thickness of ≈5 nm (Figure 2d). High-resolution TEM (HRTEM) image in Figure 2e shows clear lattice fringes with interspacing of 0.25 and 0.30 nm, corresponding to the (311) and (220) planes of cubic-phase Fe_3O_4, respectively. The single-crystalline nature of Fe_3O_4 nanorod is further evidenced by the fast Fourier transformation (FFT) pattern in Figure 2f, which clearly displays regular diffraction spots.

The composition of the Fe_3O_4–C array was examined by X-ray diffraction (XRD) and the result is shown in **Figure 3**a. In addition to the peaks from Ti substrate (JCPDS card No. 1–1198), the other sharp peaks can be well indexed to Fe_3O_4 (JCPDS card No. 3–863). No obvious signals from carbon can be detected, which is due to the partially carbonization as observed in TEM. To further determine the valence state information of the iron oxide-based hybrid array, X-ray photoelectron spectroscopy (XPS) measurements were performed. A full XPS spectrum is shown in Figure 3b, which unambiguously indicates the presence of C (from the carbon shell; inset is the C 1s core level spectrum), O and Fe elements (arising from Fe_3O_4). For the Fe 2p spectrum (Figure 3c), two peaks at binding energies of 710.8 and 724.5 eV correspond to Fe $2p_{3/2}$ and Fe $2p_{1/2}$, respectively.[28,29] The spin-orbit-split Fe2p peaks are broad due to a small chemical shift difference between Fe^{2+} and Fe^{3+} present in Fe_3O_4. Moreover, the absence of a shake-up satellite peak at ≈719.0 eV that is the fingerprint of the electronic structure of Fe_2O_3,[30] further confirms the formation of Fe_3O_4 rather than Fe_2O_3. In Figure 3d, the Fe $2p_{3/2}$ spectrum is well fitted with a major peak at 711.4 eV and a minor one at 710.0 eV, which can be ascribed to Fe^{3+} and Fe^{2+} in Fe_3O_4, respectively.

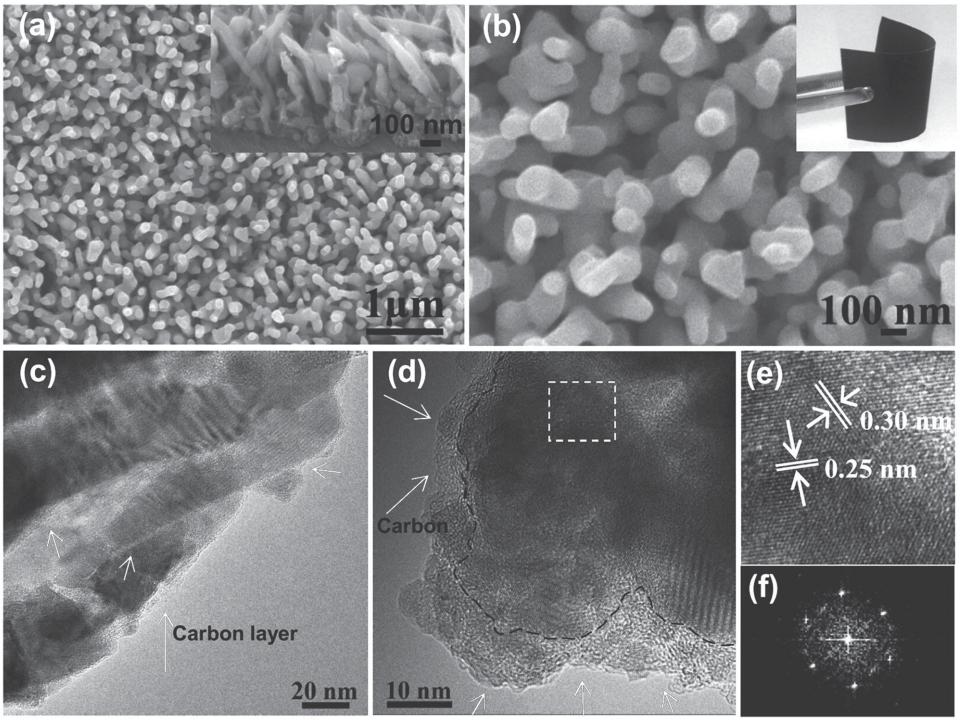

Figure 2. a,b) SEM images of the Fe_3O_4–C nanorod array (inset in (a) is the cross-sectional image; inset in (b) is the optical image). c,d) TEM images of the nanorods, showing the presence of carbon shell. e) HRTEM image and f) FFT pattern of the region denoted by the dashed square in (d).

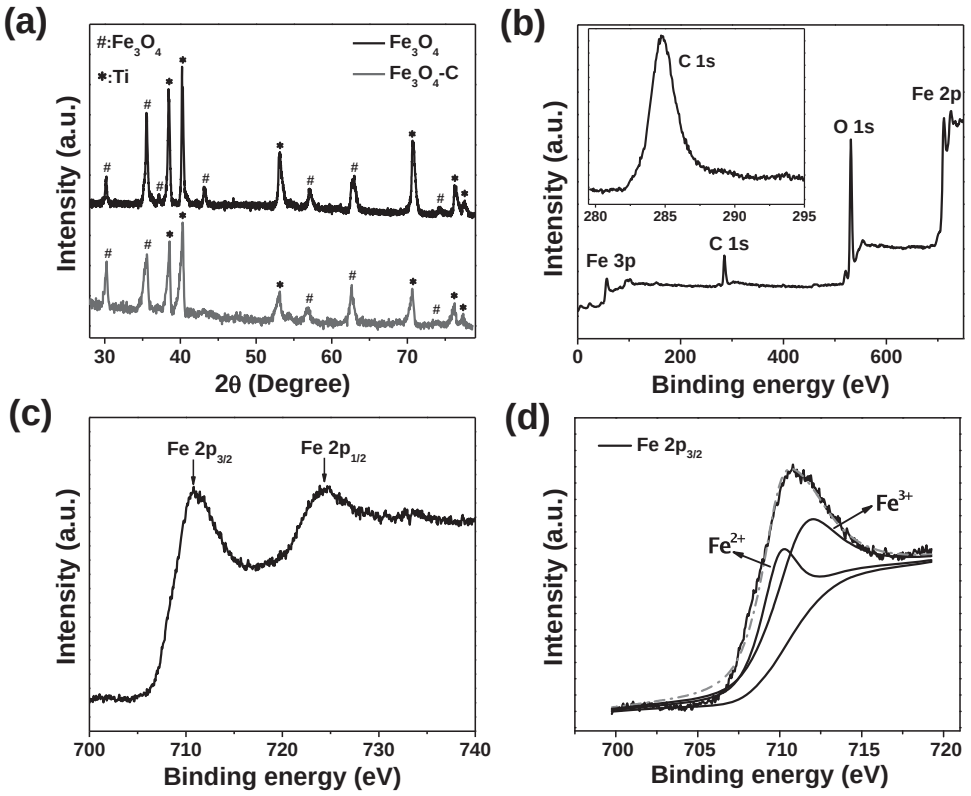

Figure 3. a) XRD patterns of Fe_3O_4 and Fe_3O_4–C nanorod arrays. b) XPS full spectrum (inset is the core level XPS spectrum for C 1s), c) XPS spectrum for Fe 2p, and d) deconvolution XPS spectrum of Fe $2p_{3/2}$ for the Fe_3O_4–C array.

2.2. Electrochemical Performance of the Fe_3O_4–C Electrode in Alkaline Electrolyte

The electrochemical studies were all conducted in a three-electrode cell using 3 M KOH aqueous electrolyte. To investigate the role of carbon shell in the Fe_3O_4–C structure, data from pristine Fe_3O_4 nanorod array electrode will also be presented in some cases for comparison.

We first unveil in detail the electrochemical behavior and redox reaction mechanism of Fe_3O_4–C array electrode in KOH solution. As shown in **Figure 4**a, multiple redox peaks appear in initial cyclic voltammogram (CV) cycles. In particular, the intensity of peaks 1, 4, and 5 increases while that of peaks 2 and 3 decreases during continuous cycling (peaks 1 and 5 grow particularly fast). After around 20 cycles, peaks 1 and 5 dominate in the CV curve, characteristic of the reversible Faradic conversion between Fe^{3+} and Fe^{2+}.[16,31] Based on the possible valence state variation of Fe, the redox reactions of peaks 1–5 are presumably assigned (Figure 4a). Accordingly, when scanned to a more negative potential approaching to hydrogen evolution, Fe^{2+} is further reduced to Fe^0 (peak 2). In reverse, Fe^0 is subsequently oxidized into Fe^{2+} with the potential swept toward the positive direction (peaks 3 and 4). To confirm the above assumption, XRD and XPS investigations were performed to indentify the component evolution at different CV stages (after 10-cycle activation; to ensure the presence of all the five peaks). The XRD patterns of the array samples with CV exactly scanned over peak 1, 2, 3, 4, and 5 are displayed in Figure 4b, respectively (clockwise scanning; denoted as Sample 1–5 for convenience). The peak at 44.66° is well corresponded to Fe (JCPDS card No. 6–696). The simultaneously appeared peaks at 44.28° and 54.38° are indexed to FeO (JCPDS card No. 49–1447), and the peak present alone at 54.38° is assigned to (116) plane of Fe_2O_3 (JCPDS card No. 84–308). In general, it is observed that during the discharging process, FeO is first generated, and then further reduced to Fe, as confirmed by the apparent intensity increase of the XRD peak at 44.66° for Sample 2. In the charging process, the oxidation of Fe^0 to FeO is not so obvious at the initial stage (from CV peak 3 to 4), possibly due to the formation of the intermediate phase $Fe(OH)_{ads}$.[32] Nevertheless, the Fe^0 can be completely oxidized to FeO_x with increasing the charging depth, as evidenced by the absence of XRD peak at 44.66° (Fe) for Sample 5 and the emergence of a much higher XRD peak at 54.38° (Fe_2O_3) as compared to that for Sample 4. Furthermore, XPS Fe $2p_{3/2}$ spectrum in Figure 4c clearly demonstrates the generation of Fe^0 with discharging depth over CV peak 2. When charging over CV peak 5, a shakeup satellite XPS peak situated at ≈719.0 eV (inset in Figure 4c) is detected, indicating that at the final CV stage the dominant surface component is Fe_2O_3. Fitting Fe $2p_{3/2}$ spectrum of Sample 5 also uncovers the presence of a small ratio of Fe^{2+} oxide, which should be further oxidized into Fe_2O_3 and contributes to the intensity increase of peak 5 upon subsequent CV sweeping.

Based on the above analysis, prior to the performance evaluation, all the Fe_3O_4-based electrodes were activated for 20 CV cycles to achieve characteristic electrochemical behavior.

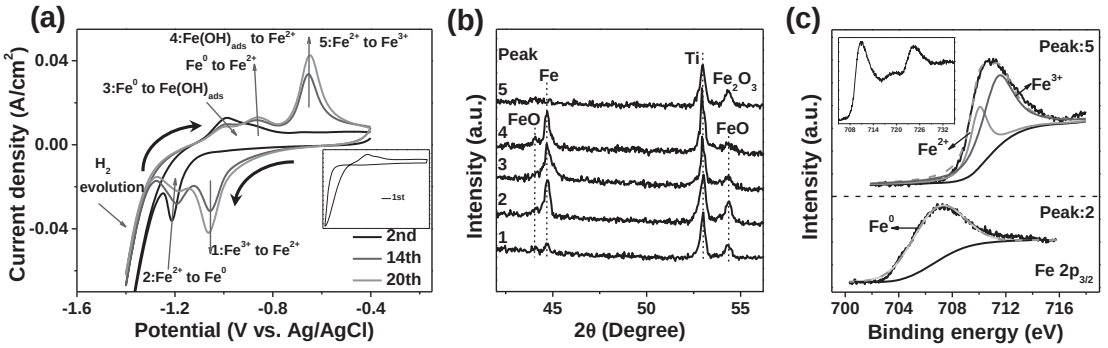

Figure 4. a) Initial CV scans of the Fe_3O_4-based electrode in 3 M KOH (inset: the first cycle). b) XRD patterns of the electrode after CV just scanning over peak 1–5, respectively. c) The deconvolution XPS Fe $2p_{3/2}$ spectra of the electrode with CV scanned over peak 2 and 5, respectively. Inset shows a shakeup satellite XPS peak observed between Fe $2p_{3/2}$ and Fe $2p_{1/2}$ after charging over peak 5.

Figure 5a,b shows the CV curves of pristine Fe_3O_4 and Fe_3O_4–C nanorod array electrodes at 5–50 mV s^{-1}, respectively. The two electrodes exhibit similar electrochemical feature, dominated by a pair of well-defined symmetric redox peaks (peak 1 and 5; $Fe^{3+} \rightleftharpoons Fe^{2}$) coexisting with other small peaks 2–4 ($Fe^{2+} \rightleftharpoons Fe^{0}$). Such profile clearly indicates that Fe_3O_4 electrodes have undergone a sufficient valence state transformation within the potential window of –1.3 to –0.5 V (vs Ag/AgCl). The increasing hysteresis between redox peaks with the increase of scan rate further reveals the battery-type electrochemical behavior. Figure 5c displays the direct CV comparison of the two Fe_3O_4 electrodes at 20 mV s^{-1}, which indicates that the Fe_3O_4 electrode exhibits more obvious redox peaks and much higher capacity after appropriate carbon modification. The stored charge was calculated for both the two electrodes and plotted as a function of scan rate, as shown in Figure 5d. As can be seen, the Fe_3O_4–C nanorod array electrode always exhibits higher capacity than the pristine Fe_3O_4 electrode. At 2 mV s^{-1}, it delivers a high capacity of 0.4278 C cm^{-2} (7776.36 C cm^{-3}, 247.5 mAh g^{-1}), nearly 30% enhancement of the pristine Fe_3O_4 electrode (0.3296 C cm^{-2}, 5992.73 C cm^{-3}, 190.7 mAh g^{-1}). The gravimetric capacity of 247.5 mAh g^{-1} has achieved 71.4% of the theoretical value, comparable to promising alkaline rechargeable battery anodes.[5,33,34] Moreover, the capacity values for our Fe_3O_4-based array electrodes are substantially larger than those reported for other typical FeO_x-based nanostructures, such as Fe_2O_3 nanotubes@graphene (0.23 C cm^{-2}, 59.72 mAh g^{-1}),[23] Fe_2O_3 nanoparticles@graphene (189.17 mAh g^{-1}),[17] Fe_3O_4 nanosheets-carbon nanofibers (37.5 mAh g^{-1}),[35] Fe_3O_4-rGO (220.43 mAh g^{-1}),[18] and Fe_3O_4@SnO_2 nanofilm (4.2 mC cm^{-2}).[27] From Figure 5d, the capacity retention for the Fe_3O_4–C array electrode is further estimated ≈41% with the scan rate increased as high as 100 times from 2 to 200 mV s^{-1} (33% for the pristine Fe_3O_4 electrode), demonstrating excellent rate performance. The above evidence implies that proper carbon shell coating might increase the electrical conductivity of the Fe_3O_4 electrode, which ensures faster and more efficient electron transport within the electrode, especially at high rates.

With optimized carbon coating (0.15 M glucose solution as precursor), the most remarkable performance improvement is the cycleability. As shown in Figure 5e, the pristine Fe_3O_4 array electrode exhibits dramatic capacity fading; merely ≈36.0% of the initial capacity can be retained after only 100 cycles. By contrast, the capacity retention of the Fe_3O_4–C array electrode remains ≈83.9% after 2000 cycles, and still 64.0% even after 5000 cycles, which demonstrates amazing enhancement of the cyclic endurance and stability. The cycling performance is much superior to those of many reported FeO_x-based electrodes such as Fe_2O_3 nanoparticles@graphene (75%, 200 cycles, in 1 M KOH),[17] Fe_3O_4@graphene (38%,1000 cycles, 1 M KOH),[18] Fe_2O_3 nanosheets/particles (60%–70%, 1000 cycles, in 1 M Li_2SO_4/Na_2SO_4),[36,37] and PANI-Fe_3O_4 composites(85%, 300 cycles, in 1 M H_2SO_4),[38] some of which were tested even in neutral electrolyte without *bulk* redox reactions.

Despite the above results, it should be noted that the concentration of carbon source (glucose) has significant influence on the cycleability of the Fe_3O_4–C electrode. As further seen in Figure 5e, although better than pristine Fe_3O_4 electrode, the capacity retention for Fe_3O_4–C samples derived from glucose solution concentration of 0.05 and 0.2 M is only ≈18.1% and 49.9% after 2000 cycles, respectively. In general, with the increase of the glucose concentration, the carbon coating amount will increase and it will be more convenient to buffer the inner volume expansion and prevent the structural pulverization of Fe_3O_4 during repeated harsh redox reactions; the electrical conductivity can be increased as well. However, too much carbon decoration might not be good for OH^- ion diffusion into the inner Fe_3O_4 nanorod; accordingly, despite that the capacity decay is slower, the real capacity is greatly reduced (with 0.20 M, the capacity of the resulting hybrid electrode is only ≈60.0% that of the pristine electrode). We speculate that for Fe_3O_4–C electrode from 0.15 M glucose solution, the surface carbon shell not only effectively buffers the volume change of Fe_3O_4 nanorods, but also guarantees the gradual penetration of OH^- ions. In accord with this, the activation of this electrode takes much longer time (up to 1000 cycles with the capacity increasing), thus pushing the electrochemical durability beyond thousands of cycles. The electrochemical impedance spectroscopy (EIS) was further utilized to support the above analysis. In the EIS spectrum, at the high frequency, the intersection of the curve at the real part indicates the resistance of the electrochemical system (R_s), while at the low frequency the slope of the spike reflects the ion diffusion. As displayed in Figure 5f, R_s indeed decreases with the carbon coating, indicative of the

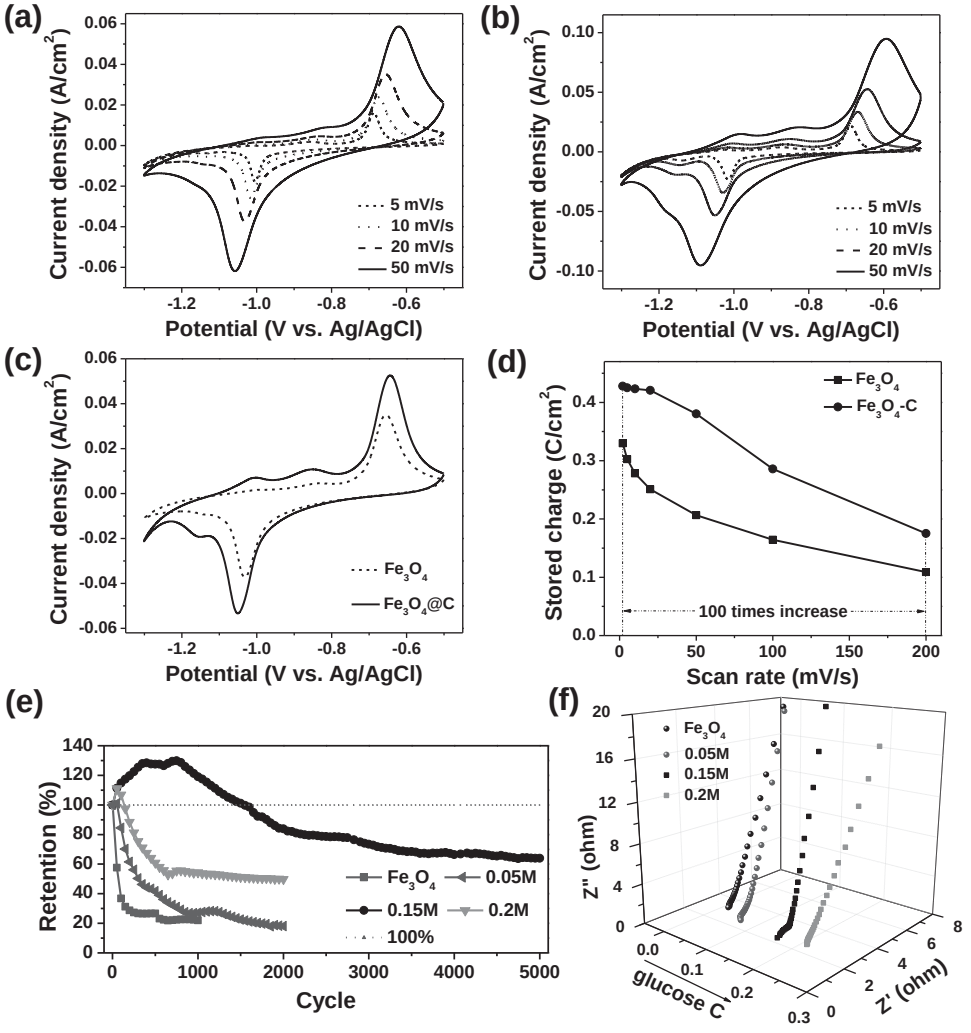

Figure 5. CV curves of a) pristine Fe_3O_4 and b) Fe_3O_4–C electrodes at various scan rates. c) CV curve comparison of the two Fe_3O_4-based electrodes at 20 mV s^{-1}. d) The stored charge/capacity as a function of scan rate for the two electrodes. e) Cycling performance and f) EIS spectra of Fe_3O_4–C electrodes fabricated from different glucose concentrations.

reduced electrical conductivity (0.15 M derived Fe_3O_4–C has the smallest R_s: 2.72 Ω; the pristine electrode: 3.43 Ω). Nevertheless, with too much carbon modification (0.20 M glucose), the derived Fe_3O_4–C electrode shows the most sluggish ion diffusion evidenced by the lowest slope of the spike, as anticipated. **Figure 6** illustrates the SEM images of pristine Fe_3O_4 and optimized (0.15 M) Fe_3O_4–C array electrodes after 1000 cycles. It is observed that the pristine Fe_3O_4 nanorods have been destroyed into numerous nanoparticles after repeated redox reaction (Figure 6a). In contrast to this, with carbon shell protection, the arrayed architecture can still be well preserved although the surface morphology of the nanorods has changed a lot (Figure 6b).

2.3. Construction and Performance of $CNTs_{(+)}//Fe_3O_4–C_{(-)}$ Hybrid Energy Storage Device

To further evaluate the optimized Fe_3O_4–C nanorod array electrode for device applications, a novel alkaline battery-supercapacitor hybrid system was designed. In such an energy storage device, catalyst-free CNTs nanofilm was chosen as the supercapacitive cathode to assemble with Fe_3O_4–C alkaline battery-type anode.

The CNTs nanofilm was grown on a 3D carbon cloth current collector via a Ni-catalytic CVD method. The catalysis nickel was further dissolved to attain Ni-free CNTs nanofilm cathode in order to avoid the redox reaction of Ni in alkaline electrolytes. **Figure 7**a displays SEM image of the homogeneously grown CNTs cathode. The inset TEM image further reveals the Ni-free and multiwalled nature of the nanotubes with 0.34 nm interplanar spacing.[39] Raman spectrum in Figure 7b demonstrates the characteristic D band (1340 cm^{-1}) and G band (1570 cm^{-1}) of graphite; the presence of D band defect peak indicates that the CNTs film is partially crystallized. Figure 7c illustrates the CV curves of both the Fe_3O_4–C anode and CNTs cathode in KOH aqueous electrolyte at 10 mV s^{-1}. Different from Fe_3O_4–C anode, the CNTs nanofilm electrode exhibits rectangular CV profile, indicative of the electric double-layer capacitive behavior. The stored charge of the two electrodes is

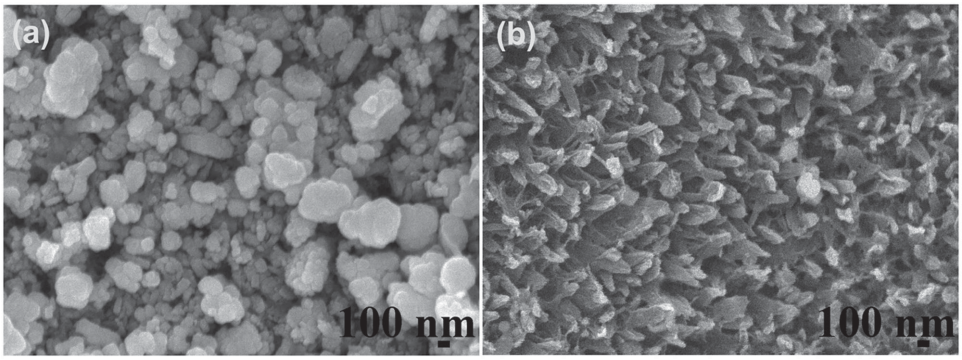

Figure 6. SEM images of a) Fe_3O_4 and b) Fe_3O_4–C electrodes after 1000 cycles in 3 M KOH electrolyte.

further calculated to be ≈0.190 and 0.196 C, demonstrating that they are well matched.

We constructed a solid-state hybrid device by using PVA-KOH gel as both the electrolyte and separator, and investigated its electrochemical performance. For comparison, hybrid device using 3 M KOH aqueous electrolyte was also assembled and evaluated. **Figure 8**a,b shows the CV curves of the aqueous electrolyte- and gel electrolyte-based hybrid devices at scan rates from 10 to 100 mV s^{-1}, respectively. The operating potential window is 0–1.7 V, comparable to typical hybrid SCs and much higher than symmetric SCs (in general <1.0 V).[40] As can be seen, both the two devices display a quasi-rectangular CV geometry without sharp redox peaks. The rate capability is also comparatively shown in Figure 8c. Interestingly, the charge stored in the solid-state hybrid device is nearly 100% of that stored in the aqueous electrolyte-based hybrid device at low scan rate (5 mV s^{-1}). At higher scan rates from 10 to 200 mV s^{-1}, however, the capacities of the solid-state device are slightly lower than those of the aqueous device. To understand the reason, EIS testing was performed and Nyquist plots of the two devices are illustrated in Figure 8d (inset is the enlarged view). Evidently, the R_s value for the aqueous device (7.3 Ω) is smaller than that of the solid-state device (7.8 Ω). Moreover, the slope of the straight line for aqueous device is much larger than that of the solid-state one, suggesting a much lower diffusion resistance. These results imply that in the quasi-solid state the charge transfer and ion diffusion should be relatively sluggish, and the interfacial contact between active materials and electrolyte is no so intimate, which definitely have essential impact on the electrochemical kinetics in case of high rates. Figure 8e,f further shows the typical discharge curves for both the devices at various current densities. The solid-state device always exhibits linear discharge profile regardless of the current density. But for the aqueous device, the discharge profile is only relatively linear at high currents; at low currents, a sloping plateau can be detected. This phenomenon might be ascribed to the fact that in aqueous electrolyte the cathode and anode are not always matched at every current rate (the difference between the rate performance of cathode and anode should be more obvious in aqueous electrolyte).

Solid-state energy storage device offers a number of desirable advantages such as the ease of scalability, improved safety and flexibility, high reliability, and so forth. Next, we will focus on the device performance of solid-state hybrid system. The structure details of the solid-state $CNTs_{(+)}//Fe_3O_4–C_{(-)}$ alkaline battery-supercapacitor hybrid device are schematically illustrated in **Figure 9**a. The thickness of the whole device is estimated as ≈360 µm (inset picture). In order to manifest the superiority of our device for thin-film energy storage, Ragone plot of volumetric energy density versus power density is presented and compared with previously reported data as well as those of commercial state-of-the-art energy storage systems (Figure 9b). Our solid-state hybrid device delivers a maximum volumetric energy density of 1.56 mWh cm^{-3} at the power density of 0.028 W cm^{-3}. The maximum energy value is considerably higher than those of the symmetric SCs[41–43] and is also much superior to those of many recent solid-state energy storage devices such as $Co_9S_8//Co_3O_4@RuO_2$ (1.21 mWh cm^{-3}),[44] $MnO_2//Fe_2O_3$ (0.41 mWh cm^{-3},[25] and 0.55 mWh cm^{-3};[45] in PVA-LiCl electrolyte), $H\text{-}TiO_2@MnO_2//H\text{-}TiO_2@C$ (0.3 mWh cm^{-3}),[46] $ZnO@MnO_2$//graphene (0.234 mWh cm^{-3}),[47] and VO_x//VN (0.61 mWh cm^{-3}).[48] It is even reaches the level of thin-film lithium battery (0.3–10 mWh cm^{-3}) and about several times that of commercial 5.5 V/100 mF SC (<0.6 mWh cm^{-3}).

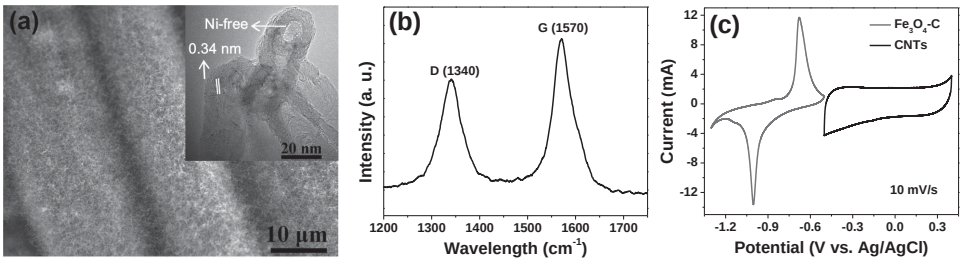

Figure 7. a) SEM image and b) Raman spectrum of CNTs nanofilm cathode. Inset in (a) is the TEM image of CNTs, showing that Ni was removed. c) Comparative CV curves of Fe_3O_4–C anode and CNTs cathode performed in a three-electrode cell in 3 M KOH.

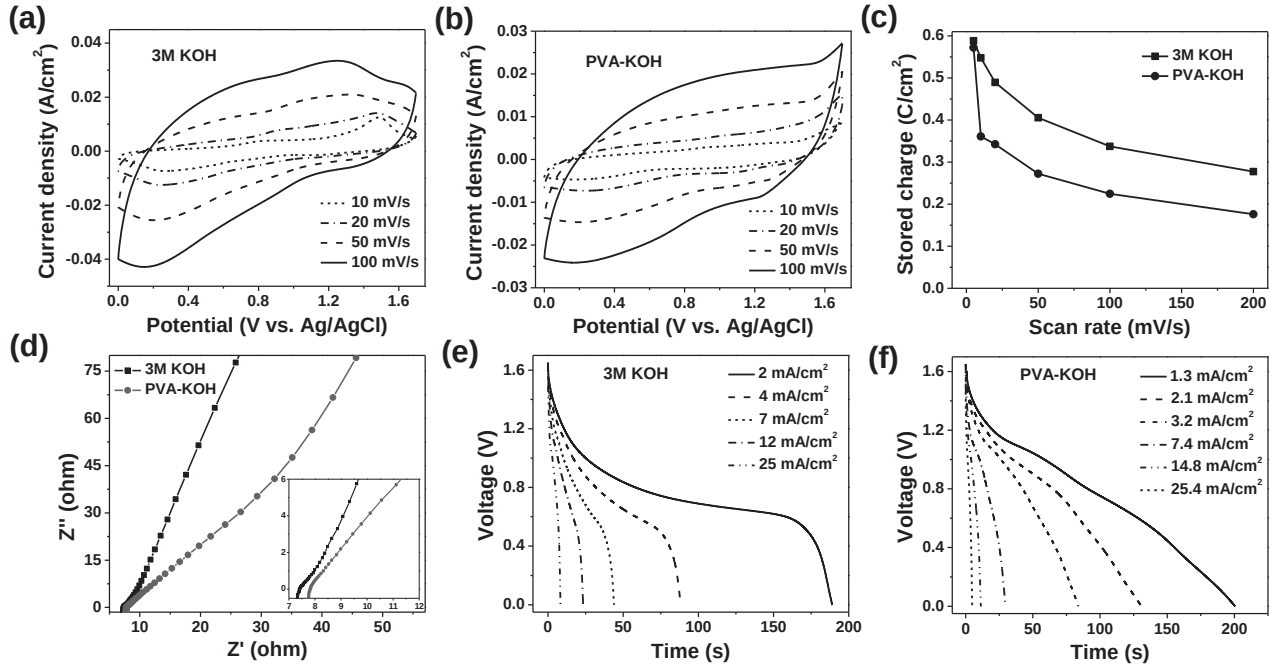

Figure 8. CV curves of a) aqueous and b) solid-state CNTs//Fe_3O_4–C hybrid devices. c) Stored charge as a function of scan rate and d) EIS spectra for both aqueous and solid-state hybrid devices. Discharge curves of e) aqueous and f) solid-state hybrid devices.

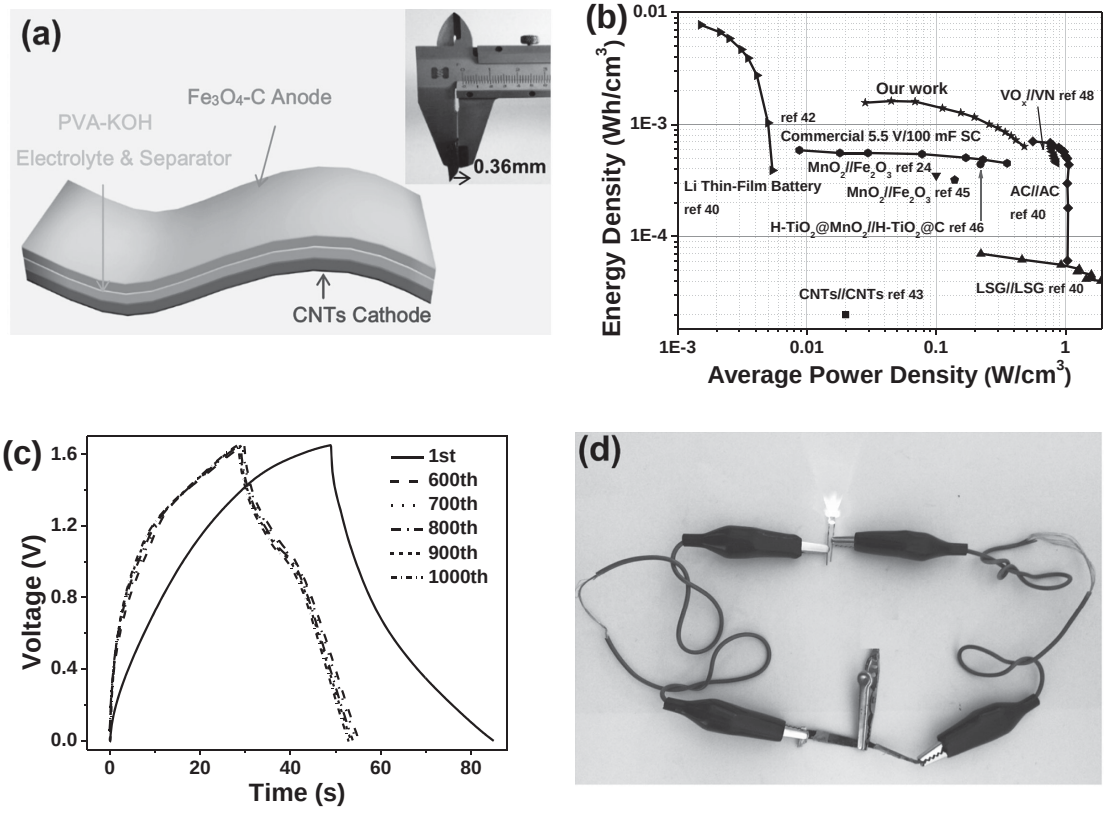

Figure 9. The CNTs//Fe_3O_4–C solid-state hybrid device: a) Schematic illustration of the device configuration. Inset is the optical image showing the thickness of device. b) The Ragone plot. c) Charge–discharge curves of the 1st and 600th–1000th cycles; d) Optical image showing two devices in series can light up the red LED indicator.

The maximum volumetric power density of our device is ≈0.48 W cm^{-3}, approaching that of the commercial AC//AC SC; it is also almost two orders of magnitude that of commercial lithium thin-film battery. At such a power density, the device is charged to full within 4.8 s but still maintains high energy density of 0.64 mWh cm^{-3}.

Cycle life of the hybrid device was further measured by galvanostatic technique at 5.5 mA cm^{-2}. The charge/discharge curves for the 1st, 600th, 700th, 800th, 900th, and 1000th cycle are displayed in Figure 9c. About ≈67.7% of the initial capacity can be maintained after 1000 cycles, demonstrating good cycling stability. It is worth mentioning that the capacity essentially keeps stable after 600 times of cycling, evidenced by the almost overlapping charge–discharge curves from the 600th to 1000th cycle. To demonstrate the potential use of our hybrid device, we connected two device units (total effective area: ≈0.8 cm^2) in series to drive a 3 mm-diameter red light-emitting-diode (LED; 1.8 V, 20 mA). After charging, the integrated device could power the LED indicator brightly, as shown in Figure 9d.

The aforementioned results clearly demonstrate that binder-free iron oxide nanostructured electrode, if properly decorated with carbon shell, can achieve greatly enhanced cycleablity in alkaline electrolyte despite of harsh bulk redox reactions. This also enables the construction of novel iron oxide alkaline battery anode-based hybrid energy storage devices with both high energy and power densities. To further understand the energy storage mechanism of our device, for CV data, we separated the surface capacitive effect and diffusion-controlled contribution from the total stored charge (capacity) using Dunn's method.[49,50] In detail, we expressed the current response at a fixed potential V as the combination of two separate mechanisms: surface capacitive effect ($k_1\nu$) and diffusion-controlled process ($k_2\nu^{1/2}$):

$$i(V) = k_1\nu + k_2\nu^{1/2}$$

where i is the current, ν is the scan rate. By determining k_1 and k_2, the fraction of the current arising from the two mechanisms at specific potentials was distinguished. As in **Figure 10**a, the pure capacitive contribution at 20 mV s^{-1} is illustrated with the shallowed area, which holds 67.8% of the total capacity. We further calculated that at even slow scan rate of 5 mV s^{-1}, the capacitive mechanism still contributes to 52.9% of the capacity (55.6% at 10 mV s^{-1}; 71.0% at 50 mV s^{-1}; 86.4% at 100 mV s^{-1}). These quantitative data are in line with our hybrid device design that integrates the alkaline battery-type (diffusion-controlled) Fe_3O_4 with the supercapative CNT, and also explain well why our device can simultaneously exhibit high energy and power densities (excellent rate performance).

Our solid-state hybrid device also has high environmental suitability. Figure 10b demonstrates that the device is flexible and can be substantially bent without essentially deteriorating the electrochemical profile and capacity (≈99.6% retention). Besides being flexibility, the device can withstand high mechanical pressures. As demonstrated in Figure 10c and its inset, even with the pressure increased up to ≈32.9 kPa, the capacity changes slightly despite of the variation at the two ends of the corresponding CV. It is believed that the PVA-KOH gel electrolyte solidifies during the device assembly and acts like glue that holds all the device components together, thus improving

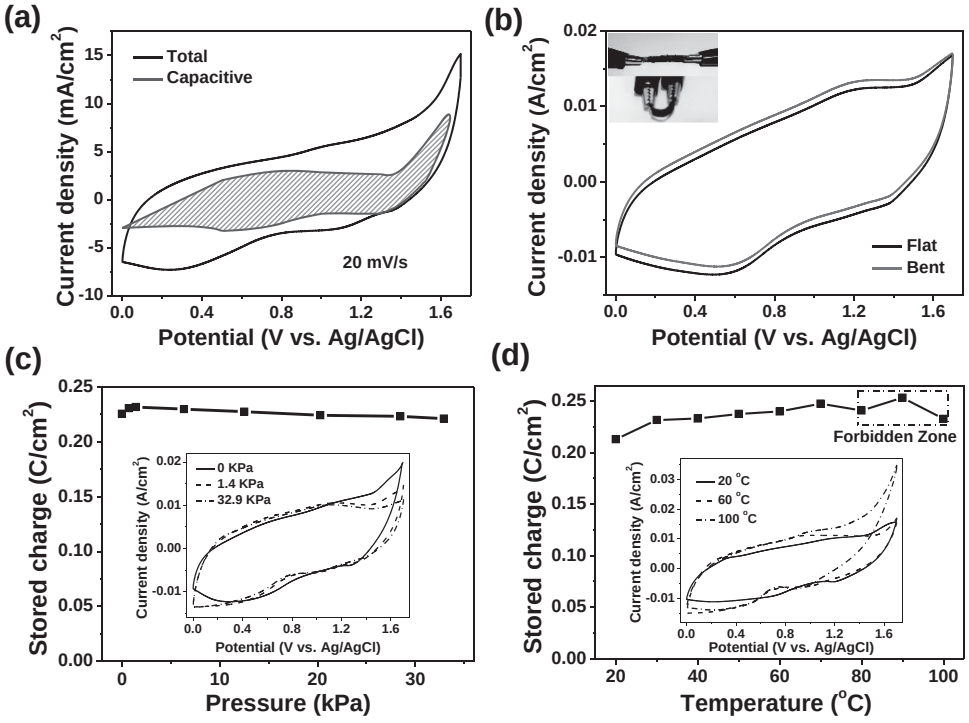

Figure 10. The CNTs//Fe_3O_4–C solid-state hybrid device: a) CV curve at 20 mV s^{-1} with shadowed area representing the capacitive contribution. b) CV curves collected under different conditions; inset is the optical images of the device at the normal and bending states. c) Plot of stored charge versus mechanical pressure. d) Stored charge variation upon the gradual increase of the temperature. Insets in (c) and (d) are the corresponding CV curves.

the mechanical integrity and stability under extreme bending and pressure conditions. The performance of our device at different environmental temperatures ranging from 20 to 100 °C was also investigated (Figure 10d and inset). As can be seen, the device capacity is relatively stable when the temperature is lower than 80 °C. With the temperature over 80 °C, the capacity value is seriously fluctuated; in this case, the device can work for only a short time and then turns to a weak state. As evidenced, the CV shape obviously changes at the high potential (1.3–1.7 V) when the operating temperature is elevated to 100 °C. Nevertheless, our device can work well within a wide temperature window of 20–80 °C. The good environmental suitability demonstrated above endows our device with great application potentials in portable/wearable electronics.

3. Conclusions

In summary, we have proposed a "carbon shell-protection" solution to remarkably improve the cycleability of the instable binder-free iron oxide alkaline battery anode from only hundreds of cycles to thousands of cycles. With excellent rate performance and a high capacity, the optimized Fe_3O_4–C nanorod array anode is assembled with directly-grown CNTs nanofilm cathode into a flexible solid-state rechargeable alkaline battery-supercapacitor hybrid device for the first time. The device is fully binder-free, exhibiting high volumetric energy density approaching commercial Li thin-film batteries and high power density comparable to commercial SCs (1.56 mWh cm^{-3}; 0.48 W cm^{-3}). It also has good cycling stability and high environmental suitability in terms of substantially bending, high mechanical pressure and elevated temperature. The "carbon shell-protection" strategy presented herein is general and can be readily applied to other metal oxide/hydroxide arrayed electrodes that are instable in aqueous electrolytes. Our work provides a facile way in exploring the application possibility of iron oxide alkaline battery anode and in developing new types of iron oxide-based energy storage devices.

4. Experimental Section

Synthesis of Fe_3O_4–C Nanorod Array Anode: The pristine Fe_3O_4 nanorod array was first fabricated via a hydrothermal and post-annealing process. Typically, 0.946 g $FeCl_3{\cdot}H_2O$ and 0.497 g Na_2SO_4 was dissolved in a 70 mL solution of distilled water. And then, the resulting solution was transferred into a Teflon-lined stainless steel autoclave with a thin Ti foil and kept at 160 °C for 6 h. The hydrothermally prepared sample on Ti foil was collected, dried, and further annealed at 600 °C in the flow of Ar gas for 2 h to obtain Fe_3O_4 nanorod array. The Fe_3O_4–C array was further synthesized by immersing the pristine array into glucose aqueous solution (0.05–0.2 M) for 24 h with subsequent carbonization (600 °C, 2 h).

Preparation of Catalyst-Free CNTs Nanofilm Cathode: The Ni-CNTs nanofilm was first fabricated by a facile CVD method. Typically, carbon cloth (CeTech, thickness: ≈0.33 mm) was infiltrated with a 0.5 M nickel nitrate hexahydrate solution and then dried. The treated carbon cloth was then put into a tube furnace and annealed at 800 °C for 30 min with a 15 mL mixed ethanol and ethylene glycol solution (the volume ratio is 1:5) placed at the tube entrance in the flow of Ar gas. Finally, to dissolve the nickel catalyst, the as-prepared Ni-CNTs nanofilm was immersed in 0.1 M $Fe(NO_3)_3$ solution for 24 h.

Characterizations: The electrode samples were characterized by using SEM (JSM-6700F), TEM (JEM-2010FEF; 200 kV), XRD (Bruker D-8 Avance), XPS (Thermo Electron, VG ESCALAB 250 spectrometer), and Raman spectroscopy (Witech CRM200 (532 nm)). The mass of the active materials was measured on an AX/MX/UMX Balance (METTLER TOLEDO, Maximum = 5.1 g; d = 0.001 mg).

Fabrication of $CNTs_{(+)}//Fe_3O_4$–$C_{(-)}$ Hybrid Devices: The aqueous device was constructed with the Fe_3O_4–C anode and CNTs cathode in opposition to each other in 3 M KOH aqueous electrolyte. To fabricate the solid-state hybrid device, the two electrodes were coated with PVA-KOH gel electrolyte and then assembled face to face for solidification. After the PVA-KOH gel solidified, it also acted as separator. The gel electrolyte was prepared as follows: 4 g PVA (1788 type) and 4 g KOH were dissolved in 40 mL distilled water with vigorously stirring for 1 h at 80 °C until a uniform sol was formed.

Electrochemical Measurements: All the electrochemical measurements were carried out using a CS310 electrochemical workstation. For individual working electrode samples, the performance was conducted in a three-electrode mode with a Pt foil as counter electrode and an Ag/AgCl as reference electrode in 3 M KOH. For device testing, a two-electrode mode was used. To investigate the pressure effect, the device was placed on a flat glass plate, and then regular iron blocks with different definite masses were added directly to the upper surface of the device one by one to generate the mechanical pressure. To investigate the temperature effect, the solid state hybrid device was placed in an oven with precise temperature control; two Cu wires were further used to connect the device with the outer Electrochemical Station.

The specific stored charge (capacity Q) can be calculated based on CV curve according to: $Q = \frac{\int I(V)\,dV}{2\upsilon A}$, where $I(V)$, dV, υ, and A represent the current at V, differential potential, scan rate, and the electrode's surface area (or mass of the active materials), respectively. The volumetric energy and power densities (E and P) of the solid-state device were calculated using $E = \frac{I\int V(t)\,dt}{T}$ and $P = E/\Delta t$, where I is the discharging current, $V(t)$ is discharging voltage at t, dt is time differential, T is the device volume, and Δt is the total discharging time.

Acknowledgements

This work was supported by grants from the National Natural Science Foundation of China (Nos. 51102105, 11104088), the Science Fund for Distinguished Young Scholars of Hubei Province (No. 2013CFA023), the Youth Chenguang Project of Science and Technology of Wuhan City (No. 2014070404010206), Self-determined Research Funds of CCNU from the Colleges' Basic Research and Operation of MOE (CCNU14A02001), the Self-determined Innovation Foundation of Huazhong University of Science and Technology (No. 2013027), and the Research Start-Up Fund from Wuhan University of Technology.

Received: June 3, 2015
Revised: July 2, 2015
Published online: July 29, 2015

[1] a) J. R. Miller, P. Simon, *Science* **2008**, *321*, 651; b) M. H. Yu, Y. C. Huang, C. Li, Y. X. Zeng, W. Wang, Y. Li, P. P. Fang, X. H. Lu, Y. X. Tong, *Adv. Funct. Mater.* **2015**, *25*, 324.

[2] a) J. Liu, Y. R. Wen, Y. Wang, P. A. Aken, J. Maier, Y. Yu, *Adv. Mater.* **2014**, *26*. 6025; b) J. M. Tarascon, M. Armand, *Nature* **2001**, *414*, 359; c) J. F. Ni, Y. Zhao, T. T. Liu, H. H. Zheng, L. J. Gao, C. L. Yan, L. Li, *Adv. Energy Mater.* **2014**, *4*, 1400798; d) Y. Jiang, Z. Z. Yang, W. H. Li, L. C. Zeng, F. S. Pan, M. Wang, X. Wei, G. T. Hu, L. Gu, Y. Yu, *Adv. Energy Mater.* **2015**, *5*, 1402104.

[3] a) G. Liu, L. C. Yin, J. Pan, F. Li, L. Wen, C. Zhen, H. M. Cheng, *Adv. Mater.* **2015**, *27*, 3507; b) G. Yu, X. Xie, L. Pan, Z. Bao, Y. Cui,

Nano Energy **2013**, *2*, 213; c) M. Huang, Y. Zhang, F. Li, L. Zhang, R. S. Ruoff, Z. Wen, Q. Liu, *Sci. Rep.* **2014**, *4*, 3878; d) J. Yan, Q. Wang, T. Wei, Z. J. Fan, *Adv. Energy Mater.* **2014**, *4*, 1300816.
[4] H. Kim, M. Y. Cho, M. H. Kim, K.Y. Park, H. Gown, Y. S. Lee, K. C. Roh, K. Kang, *Adv. Energy Mater.* **2013**, *3*, 1500.
[5] J. L. Liu, M. H. Chen, L. L. Zhang, J. Jiang, J. X. Yan, Y. Z. Huang, J. Y. Lin, H. J. Fan, Z. X. Shen, *Nano Lett.* **2014**, *14*, 7180.
[6] Y. Wang, Y. Xia, *Electrochem. Commun.* **2004**, *7*, 1138.
[7] a) Q. Wang, Z. H. Wen, J. H. Li, *Adv. Funct. Mater.* **2006**, *16*, 2141; b) C. L. Yan, W. Xi, W. P. Si, J. W. Deng, O. G. Schmidt, *Adv. Mater.* **2013**, *25*, 539; c) R. Yi, S. Chen, J. X. Song, M. L. Gordin, A. Manivannan, D. H. Wang, *Adv. Funct. Mater.* **2014**, *24*, 7433.
[8] R. T. Wang, J. W. Lang, P. Zhang, Z. Y. Lin, X. B. Yan, *Adv. Funct. Mater.* **2015**, *25*, 2270.
[9] a) H. Gwon, J. Hong, H. Kim, D. H. Seo, S. Jeon, K. Kang, *Energy Environ. Sci.* **2014**, *7*, 538; b) L. Y. Yuan, X. H. Lu, X. Xiao, T. Zhai, J. J. Dai, F. C. Zhang, B. Hu, X. Wang, L. Gong, J. Chen, C. G. Hu, Y. X. Tong, J. Zhou, Z. L. Wang, *ACS Nano* **2012**, *6*, 656.
[10] a) E. Lim, H. Kim, C. Jo, J. Chun, K. Ku, S. Kim, H. Lee, I. Nam, S. Yoon, K. Kang, J. Lee, *ACS Nano* **2014**, *8*, 8968; b) S. H. Liu, Z. Y. Wang, C. Yu, H. B. Wu, G. Wang, Q. Dong, J. S. Qiu, X. W. Lou, *Adv. Mater.* **2013**, *25*, 3462; c) Z. Yuan, H. J. Peng, J. Q. Huang, X. Y. Liu, D. W. Wang, X. B. Cheng, Q. Zhang, *Adv. Funct. Mater.* **2014**, *24*, 6105.
[11] a) P. H. Yang, W. J. Mai, *Nano Energy* **2014**, *8*, 274; b) J. W. Zhao, S. M. Xu, K. Tschulik, R. G. Compton, M. Wei, D. O'Hare, D. G. Evans, X. Duan, *Adv. Funct. Mater.* **2015**, *25*, 2745.
[12] M. Beidaghi, Y. Gogotsi, *Energy Environ. Sci.* **2014**, *7*, 867.
[13] G. M. Zhou, F. Li, H. M. Cheng, *Energy Environ. Sci.* **2014**, *7*, 1307.
[14] a) M. Sasidharan, N. Gunawardhana, M. Yoshio, K. Nakashima, *Ionics* **2013**, *19*, 25; b) W. M. Zhang, X. L. Wu, J. S. Hu, Y. G. Guo, L. J. Wan, *Adv. Funct. Mater.* **2008**, *18*, 3941.
[15] S. Hussain, K. Hess, J. Gearhart, K. Geiss, J. Schlager, *Toxicol. In Vitro* **2005**, *19*, 975.
[16] a) H. L. Wang, Y. Y. Liang, M. Gong, Y. G. Li, W. Chang, T. Mefford, J. Zhou, J. Wang, T. Regier, F. Wei, H. J. Dai, *Nat Commun.* **2012**, *3*, 917; b) C. L. Long, T. Wei, J. Yan, L. L. Jiang, Z. J. Fan, *ACS Nano* **2013**, *7*, 11325.
[17] H. W. Wang, Z.J. Xu, H. Yi, H. Wei, Z. H. Guo, X. F. Wang, *Nano Energy* **2014**, *7*, 86.
[18] T. W. Lin, C. S. Dai, K. C. Hung, *Sci. Rep.* **2014**, *4*, 7274.
[19] W. H. Shi, J. Zhu, D. H. Sim, Y. Y. Tay, Z. Lu, X. Zhang, Y. Sharma, M. Srinivasan, H. Zhang, H. H. Hng, Q. Yan, *J. Mater. Chem.* **2011**, *21*, 3422.
[20] X. Zhao, C. Johnston, P. S. Grant, *J. Mater. Chem.* **2009**, *19*, 8755.
[21] X. J. Zhu, Y. W. Zhu, S. Murali, M. D. Stollers, R. S. Ruoff, *ACS Nano* **2011**, *5*, 3333.
[22] a) Q. T. Qu, S. B. Yang, X. L. Feng, *Adv. Mater.* **2011**, *23*, 5574; b) G. X. Wang, H. Liu, J. Liu, S. Z. Qiao, G. Q. Lu, P. Munroe, H. Ahn, *Adv. Mater.* **2010**, *22*, 4944; c) H. Xia, C. Y. Hong, B. Li, B. Zhao, Z. X. Lin, M. B. Zheng, S. V. Savilov, S. M. Aldoshin, *Adv. Funct. Mater.* **2015**, *25*, 627.
[23] K. K. Lee, S. Deng, H. M. Fan, S. Mhaisalkar, H. R. Tan, E. S. Tok, K. P. Loh, W. S. Chin, C. H. Sow, *Nanoscale* **2012**, *4*, 2958.
[24] a) J. Jiang, Y. Y. Li, J. P. Liu, X. T. Huang, C. Z. Yuan, X. W. Lou, *Adv. Mater.* **2012**, *24*, 5166; b) C. Zhou, Y. W. Zhang, Y. Y. Li, J. P. Liu, *Nano Lett.* **2013**, *13*, 2078; c) B. L. Ellis, P. Knauth, T. Djenizian, *Adv. Mater.* **2014**, *26*, 3368.
[25] X. H. Lu, Y. X. Zeng, M. H. Yu, T. Zhai, C. L. Liang, S. L. Xie, M. Balogun, Y. X. Tong, *Adv. Mater.* **2014**, *26*, 3148.
[26] a) X. F. Wang, X. H. Lu, B. Liu, D. Chen, Y. X. Tong, G. Z. Shen, *Adv. Mater.* **2014**, *26*, 4763; b) L. F. Shen, E. Uchaker, X. G. Zhang, G. Z. Cao, *Adv. Mater.* **2012**, *24*, 6502; c) D. Z. Kong, J. S. Luo, Y. L. Wang, W. N. Ren, T. Yu, Y. S. Luo, Y. P. Yang, C. W. Cheng, *Adv. Funct. Mater.* **2014**, *24*, 3815.
[27] R. Z. Li, X. Ren, F. Zhang, C. Du, J. P. Liu, *Chem. Commun.* **2012**, *48*, 5010.
[28] W. Wei, S. B. Yang, H. X. Zhou, I. Lieberwirth, X. L. Feng, K. Müllen, *Adv. Mater.* **2013**, *25*, 2909.
[29] S. Tiwari, R. Prakash, R. J. Choudhary, D. M. Phase, *J. Phys. D: Appl. Phys.* **2007**, *40*, 4943.
[30] T. Fujii, F. M. F. de Groot, G. A. Sawatzky, F. C. Voogt, T. Hibma, K. Okada, *Phys. Rev. B* **1999**, *59*, 3195.
[31] P. Periasamy, B. R. Babu, S. V. Iyer, *J. Power Sources* **1996**, *58*, 35.
[32] C. Y. Kao, Y. R. Tsai, K. S. Chou, *J. Power Sources* **2011**, *196*. 5746.
[33] a) X. Y. Zhao, L. Q. Ma, X. D. Shen, *J. Mater. Chem.* **2012**, *22*, 277; b) X. P. Gao, S. M. Yao, T. Y. Yan, Z. Zhou, *Energy Environ. Sci.* **2009**, *2*, 502.
[34] a) Z. Q. Wang, Z. Q. Wu, N. Bramnik, S. Mitra, *Adv. Mater.* **2014**, *26*, 970; b) A. M. Gaikwad, A. M. Zamarayeva, J. Rousseau, H. Chu, I. Derin, D. A. Steingart, *Adv. Mater.* **2012**, *24*, 5071.
[35] J. Mu, B. Chen, Z. Guo, M. Zhang, Z. Zhang, P. Zhang, C. Shao, Y. Liu, *Nanoscale* **2011**, *3*, 5034.
[36] D. W. Wang, Q. H. Wang, T. M. Wang, *Nanotechnology* **2011**, *22*, 135604.
[37] S. P. Pang, W. H. Khoh, S. F. Chin, *J. Mater. Sci.* **2010**, *45*, 5598.
[38] S. Radhakrishnan, S. Prakash, C. R. K. Rao, M. Vijayan, *Electrochem. Solid-State Lett.* **2009**, *12*, A84.
[39] W. H. Zuo, C. Wang, Y. Y. Li, J. P. Liu, *Sci. Rep.* **2015**, *5*, 7780.
[40] D. S. Yu, K. L. Goh, H. Wang, L. Wei, W. C. Jiang, Q. Zhang, L. M. Dai, Y. Chen, *Nat. Nabotechnol.* **2014**, *9*, 555.
[41] M. F. El-Kady, V. Strong, S. Dubin, R. B. Kaner, *Science* **2012**, *335*, 1326.
[42] X. H. Lu, G. M. Wang, T. Zhai, M. H. Yu, S. L. Xie, Y. C. Ling, C. L. Liang, Y. X. Tong, Y. Li, *Nano Lett.* **2012**, *12*, 5376.
[43] M. Kaempgen, C. K. Chan, J. Ma, Y. Cui, G. Gruner, *Nano Lett.* **2009**, *9*, 1872.
[44] J. Xu, Q. Wang, X. Wang, Q. Xiang, B. Liang, D. Chen, G. Shen, *ACS Nano* **2013**, *7*, 5453.
[45] P. H. Yang,Y. Ding, Z. Y. Lin, Z. W. Chen, Y. Z. Li, P. F. Qiang, M. Ebrahimi, W. J. Mai, C. P. Wong, Z. L. Wang, *Nano Lett.* **2014**, *14*, 731.
[46] X. H. Lu, M. H. Yu, G. M. Wang, T. Zhai, S. L. Xie, Y. C. Ling, Y. X. Tong, Y. Li, *Adv. Mater.* **2013**, *25*, 267.
[47] W. Zilong, Z. Zhu, J. Qiu, S. Yang, *J. Mater. Chem. C* **2014**, *2*, 1331.
[48] X. H. Lu, M. H. Yu, T. Zhai, G. M. Wang, S. L. Xie, T. Y. Liu, C. L. Liang, Y. X. Tong, Y. Li, *Nano Lett.* **2013**, *13*, 2628.
[49] J. Wang, J. Polleux, J. Lim, B. Dunn, *J. Phys. Chem. C* **2007**, *111*, 14925.
[50] T. Brezesinski, J. Wang, S.H. Tolbert, B. Dunn, *Nat. Mater.* **2010**, *9*, 146.